photonics

MDPI

Article

Optimization of Coronary Artery Calcium Scoring Accuracy in Low-Dose Chest Computed Tomography Using Fast Non-Local Means Denoising with High-Pitch Acquisition and Tin Filtration

Jina Shim [1], Ji-Youn Kim [2,*,†] and Kyuseok Kim [3,*,†]

[1] Department of Radiological Science, Wonkwang University, 460, Iksan-daero, Iksan 54538, Republic of Korea; eoeornfl1@wku.ac.kr
[2] Department of Dental Hygiene, Gachon University, 191, Hambakmoero, Yeonsu-gu, Incheon 21936, Republic of Korea
[3] Institute of Human Convergence Health Science, Gachon University, 191, Hambakmoero, Yeonsu-gu, Incheon 21936, Republic of Korea
* Correspondence: hoho6434@gachon.ac.kr (J.-Y.K.); kskim502@gachon.ac.kr (K.K.); Tel.: +82-32-820-4376 (J.-Y.K.); +82-32-820-4360 (K.K.)
† The authors contributed equally to this work as corresponding authors.

Abstract

This study evaluated quantitative accuracy of the coronary artery calcium score (CACS) and the associated radiation dose reduction achieved by applying the fast non-local means (FNLM) algorithm to non-electrocardiography (ECG)-gated, low-dose chest computed tomography (CT) images acquired with a high-pitch scan and tin filter. Thirty patients underwent standard-dose CACS and low-dose chest CT were retrospectively analyzed. The processed low-dose images using the FNLM algorithm demonstrated a 4.2–5.0% mean CACS decrease and $\leq$16.4% median value increase relative to the standard-dose CACS CT but without statistical significance ($p > 0.05$). Notably, the quantitative error progressively decreased with increasing algorithm strength. The Pearson correlation coefficient reached 0.949 at Stage 3, indicating robust agreement with the standard-dose CACS CT. When stratified by patient heart rate, the high heart rate cohort exhibited the largest scoring errors but without statistical significance ($p > 0.05$). Importantly, the FNLM-processed protocol substantially reduced radiation dose, decreasing the mean volume CT dose index by 71.2% and dose-length product by 56.5% ($p < 0.05$). FNLM proves to be an effective post-processing technique that preserves CACS accuracy in non-ECG-gated, low-dose chest CT, thereby offering a clinically viable alternative imaging protocol for patients requiring routine screening.

Keywords: coronary artery calcium score; low-dose chest CT; fast non-local means; noise reduction; high-pitch CT; tin filter; radiation dose reduction

Check for updates

Received: 3 April 2026
Revised: 2 May 2026
Accepted: 13 May 2026
Published: 14 May 2026

Copyright: © 2026 by the authors. Licensee MDPI, Basel, Switzerland. This article is an open access article distributed under the terms and conditions of the Creative Commons Attribution (CC BY) license.

1. Introduction

Coronary artery calcification is recognized as a major biological marker of atherosclerotic lesions and plays a critical role in risk assessment and long-term prediction of clinical prognosis in coronary artery disease. The Coronary Artery Calcium Score (CACS), in particular, has been established as a robust method for objectively assessing cardiovascular event risk within asymptomatic cohorts [1–3]. Large-scale epidemiological studies consistently link higher calcification scores to an elevated probability of major cardiac events [4–8], prompting recent cardiovascular disease prevention guidelines to actively advocate for

regular screening [9]. However, in patients requiring frequent follow-ups, cumulative radiation exposure is a potential risk factor that cannot be overlooked [10,11].

To reduce radiation exposure, low-dose computed tomography (CT) protocols are increasingly adopted in various clinical settings [12–15]. Although these protocols substantially reduce the radiation dose compared with conventional chest imaging, they inherently elevate image noise, which can compromise the quantitative assessment of microlesions [16]. This increased noise becomes particularly problematic when evaluating small or low-density calcified lesions, potentially disrupting the quantitative accuracy of the CACS and the reliability of image interpretation [17–19]. Accordingly, there is a need for image postprocessing technologies that can effectively reduce noise while decreasing radiation dose [20–22].

The fast non-local means (FNLM) algorithm has recently emerged as a promising noise-reduction technique. By leveraging both spatial proximity and pixel similarity, FNLM selectively filters noise while preserving essential structural details [20]. Several previous studies demonstrated that the FNLM algorithm significantly enhances chest CT image quality and is particularly effective in maintaining fine structures in low-dose acquisitions [23,24]. However, systematic investigations into FNLM impact on quantitative evaluation metrics such as CACS remain scarce. Because algorithm application can affect different types of calcifications such as small- or low-density lesions, comprehensive studies are necessary to validate its effect on CACS accuracy [25].

Simultaneously, protocols combining high-pitch scanning with a tin (Sn) filter have gained traction for facilitating stable calcification scoring without electrocardiography (ECG) gating. High-pitch acquisitions minimize motion artifacts resulting from coronary pulsation by acquiring images in a very short timeframe, which is highly beneficial for patients presenting with irregular heart rates [26–29]. The addition of a tin filter effectively removes low-energy X-ray photons, simultaneously suppressing image noise, enhancing soft-tissue contrast, and lowering the overall patient dose [12]. Theoretically, these conditions enable accurate calcium scoring without ECG synchronization, presenting a highly useful alternative for the older adults or patients requiring repeated scans. Therefore, it was hypothesized that by combining high-pitch scanning and a tin filter during image acquisition with the FNLM algorithm, the CACS accuracy would be maintained, whereas radiation exposure would be significantly reduced.

This study aimed to determine whether the radiation dose can be safely reduced without compromising quantitative consistency by comparing the CACS derived from low-dose chest CT (acquired via high-pitch and tin filters and subsequently processed with FNLM in varying stages) against the CACS obtained through conventional standard-dose CACS CT.

2. Materials and Methods

2.1. Study Subjects

This single-center retrospective study evaluated 30 patients who underwent low-dose chest CT using high-pitch and tin filters and standard-dose CACS CT at the same institution between May 2020 and December 2023. The study protocol was approved by the Institutional Review Board of Yonsei University Health System (Approval No. 4-2024-0123), and the requirement for informed consent was waived due to the retrospective design of the study. The interval between the two examinations was strictly limited to a maximum of 6 months to minimize any potential longitudinal lesion variations. Patients with lesions currently under treatment, as well as cases in which beam hardening or metal artifacts limited image interpretation, were excluded. The cohort comprised 18 males and 12 females, with a mean age of 73.7 years (range: 60–88 years) and a mean body mass index

of 24 (range: 17.4–32). The mean heart rate during standard-dose CACS CT acquisition varied between 44 and 88 bpm (minimum range: 27–77 bpm; maximum range: 45–260 bpm). The patients were subsequently classified into three subgroups based on their mean heart rate: low (<60 bpm; n = 17), intermediate (60–80 bpm; n = 11), and high (>80 bpm; n = 2). Due to the extremely limited sample size (n = 2), the results of the high-heart-rate subgroup should be interpreted with caution, and no definitive conclusions can be drawn from this subgroup analysis. The perfect correlation observed in this subgroup is likely influenced by the small sample size and should not be interpreted as evidence of robustness.

2.2. Image Acquisition

Low-dose chest CT images were acquired using a Somatom Definition Force Scanner (Siemens Healthcare, Forchheim, Germany). Patients were positioned supine and feet-first in the gantry with both arms raised above the head to avoid anatomical interference. Proper centering at the isocenter was ensured for all subjects. The acquisition utilized a tube voltage of 100 kV, with the tube current automatically modulated based on the patient's habitus. The scanning parameters were set to a rotation time of 0.25 s, slice thickness of 1.0 mm with a 1.0 mm increment, craniocaudal scan direction, and a Br 40 reconstruction kernel. The pitch was set to 2.5, and a tin filter was applied. The scanning parameters are listed in Table 1. The anatomical scan range was extended from the lung apex to the costophrenic angle (CPA), and no intravenous contrast agent was administered.

Table 1. Scan parameters for standard-dose CACS CT and low-dose chest CT.

	Standard-Dose CACS CT	**Low-Dose Chest CT**
kVp	100	100
Eff.mAs	80	Caredose4D
Pitch	-	2.5
Sn filter	-	Use
Rotation time (s)	0.25	0.25
Slice thickness (mm)	3.0	1.0
Increment (mm)	1.5	1.0
Scan mode	Sequence	Helical
Direction	Craniocaudal	Craniocaudal

Standard-dose CACS CT images were acquired using the same scanner. The patients were positioned precisely at the isocenter with both arms raised above the head to exclude them from the scan field. The examination was conducted with ECG leads attached to the right and left shoulders, as well as the right and left lower rib cages. Images were acquired using a prospective ECG-gating method. For patients with a heart rate of 70 bpm or below, scanning was triggered at 75% of the R-R interval (mid-diastolic phase), whereas for those exceeding 70 bpm, it was triggered at 45% of the R-R interval (end-systolic phase). The protocol included a tube voltage of 100 kV, a fixed tube current of 80 mA, a rotation time of 0.25 s, a slice thickness of 3.0 mm with a 1.5 mm increment, craniocaudal direction, and an Sa36 reconstruction kernel. The scan range covered the lung apex to the CPA without contrast enhancement. Radiation dose metrics, specifically the CT dose index (CTDIvol) and dose-length product (DLP), were extracted from the dose reports for both protocols. Additionally, all ECG reports from the standard-dose CACS CT were archived to document the minimum and maximum heart rates for each examination.

2.3. Fast Non-Local Means Algorithm Modeling

In this study, FNLM algorithm was employed to reduce noise while preserving the structural details in low-dose CT images. FNLM is an accelerated version of the conven-

tional non-local means (NLM) algorithm that exploits the redundancy of similar patterns across the entire image, rather than relying solely on local neighborhoods [30].

Let $f(i)$ denote a noisy image defined on a discrete domain Ω. The restored intensity at pixel i, denoted as $g_{NLM}(i)$, is computed as the weighted average of all pixels within a predefined search window $N(i)$:

$$g_{NLM}(i) = \frac{1}{Z(i)} \sum_{j \in N(i)} w(i,j) f(j), \tag{1}$$

where $Z(i)$ is a normalization constant defined as:

$$Z(i) = \sum_{j \in N(i)} w(i,j). \tag{2}$$

The weight $w(i,j)$ reflects the similarity between two image patches centered at pixels i and j and is defined using the squared Euclidean distance between patches:

$$w(i,j) = \exp\left(-\frac{\left\|k_i - k_j\right\|_2^2}{h^2}\right), \tag{3}$$

where k_i and k_j denote vectorized image patches and h is the smoothing parameter controlling the degree of filtering [31]. This formulation assigns larger weights to pixels with similar neighborhoods and smaller weights to those with dissimilar neighborhoods, enabling effective noise reduction while preserving edges and fine structures.

Despite its effectiveness, the conventional NLM algorithm suffers from high computational complexity owing to exhaustive pairwise comparisons between patches, with a complexity on the order of $O(M^2)$ for an image with M pixels [30]. To address this limitation, the FNLM algorithm introduces several acceleration strategies. First, FNLM reduces computational burden by transforming the weight calculation from a two-dimensional (2D) patch comparison into a simplified one-dimensional (1D) representation. The modified weight function can be expressed as:

$$w(i,j) = \frac{1}{Z(i)} S(f(i+P) - f(i-P)), \tag{4}$$

where P denotes the neighborhood size and $S(\cdot)$ represents a similarity function approximating the patch distance. Here $S(\cdot)$ denotes an approximate similarity function used in the FNLM framework to reduce computational complexity. Unlike the exact squared Euclidean distance defined in Equation (3), this function is derived from simplified representations of image patches, such as reduced-dimensional features or statistical descriptors. Second, FNLM employs pre-classification of patches to exclude dissimilar neighborhoods prior to weight computation. This was achieved by comparing the statistical moments (mean, variance, and skewness) of the image patches. If the difference between the patches, defined based on the squared Euclidean distance in Equation (3), exceeds predefined thresholds, the corresponding weight is set to zero.

$$w(i,j) = 0, \ when \ \left|k_i - k_j\right| > \Delta_k. \tag{5}$$

This strategy reduces unnecessary computations and prevents bias from aggregating weakly similar patches. Third, the computational efficiency is further improved by exploiting the symmetry of the weights, which effectively halves the number of required computations. In addition, lookup tables are used to accelerate the exponential weight calculations.

The FNLM parameters were determined through a preliminary grid search to balance the noise reduction and structural preservation. Patch sizes ranging from 5×5 to 11×11

and search-window sizes ranging from 15 × 15 to 27 × 27 were evaluated. Based on this optimization, a patch size of 7 × 7 and a search window of 21 × 21 were selected as these parameters provided stable calcium lesion morphology while minimizing Hounsfield Units (HU) distortion and variability in calcium scoring. The smoothing parameter h, which governs the strength of noise suppression, was evaluated over the range of 0.0005–0.02. Three representative values were selected to define the different filtering intensities: FNLM stage 1 (low smoothing, h = 0.001), FNLM stage 2 (moderate smoothing, h = 0.005), and FNLM stage 3 (high smoothing, h = 0.01). The smoothing parameter h was selected based on its proportional relationship to the measured noise amplitude, with values corresponding approximately to 0.3×, 1.0×, and 2.5× of the noise level to define three distinct FNLM stages [25]. These parameter values were selected based on a preliminary optimization process that evaluated the trade-off between noise suppression and preservation of calcification morphology, ensuring stable quantitative performance across different filtering strengths. The FNLM algorithm was applied to the low-dose CT images using the optimized parameter set described above. All parameters, except the smoothing parameter h, were kept constant throughout the experiments to ensure consistent evaluation. The effects of different FNLM stages were assessed by comparing the resulting images and derived calcium scores. The use of multiple FNLM stages allows for a systematic evaluation of the trade-off between noise reduction and structural preservation. Increasing the smoothing parameter h enhances noise suppression but may lead to partial blurring of fine structures. Therefore, three discrete stages were defined to identify the optimal balance between image quality improvement and quantitative accuracy.

2.4. Calcium Scoring

Image analysis was conducted using Syngo.via software (VB80, Siemens Healthineers, Erlangen, Germany) by two independent radiologic technologists with 15 and 5 years of clinical experience, respectively. All data were strictly anonymized prior to assessment. All image datasets (standard-dose CACS CT and FNLM-processed low-dose CT images) were anonymized and randomized using a computer-generated sequence. Each dataset was presented independently in a randomized order, and the readers were blinded to patient identity, acquisition protocol, and processing conditions. This approach was used to minimize potential recall bias and ensure unbiased comparison across imaging conditions. Regional analysis targeted the Left Main Trunk (LM), Left Anterior Descending Artery (LAD), Circumflex Artery (CX), and Right Coronary Artery (RCA). The CACS was calculated based on the area of calcium deposition exceeding a predefined threshold of 130 HU.

2.5. Statistical Analysis

Statistical analyses were performed using SPSS version 21.0 (SPSS Inc., Chicago, IL, USA), with significance assessed at 95% confidence interval. To assess interobserver reliability, the intraclass correlation coefficient (ICC) was calculated for the CACS values measured by two radiologic technologists on the low-dose chest CT images across varying FNLM stages. The Shapiro–Wilk test indicated that the CACS data were not normally distributed; therefore, non-parametric methods were employed. The Wilcoxon signed-rank test was used to compare differences in CACS between the standard-dose and low-dose chest CT images processed at each FNLM stage (stages 1, 2, and 3) and to compare radiation dose metrics (CTDIvol and DLP). To evaluate the consistency of the CACS measurements between the FNLM-processed low-dose chest CT and standard-dose CACS CT images, Pearson correlation coefficients were calculated. Additionally, the mean absolute error (MAE) was used to assess the magnitude of error between the CACS of the FNLM-processed

images and standard-dose CACS CT. Finally, a Pearson correlation analysis was performed to evaluate the correlation between the variations in radiation dose (CTDIvol and DLP) and the absolute error of the FNLM-derived CACS, integrating all algorithmic stages. Statistical significance was set at $p < 0.05$.

3. Results

3.1. Evaluation of Accuracy and Quantitative Agreement of Calcification Scores

The interobserver reliability of the CACS measurements derived from the FNLM-processed low-dose images was highly consistent. The ICC for FNLM stages 1, 2, and 3 were 0.812, 0.823, and 0.857, respectively ($p < 0.001$).

Figure 1 illustrates the standard-dose CACS CT images alongside the low-dose chest CT images processed through varying FNLM stages for 30 subjects. As shown in Figure 2, the mean CACS for FNLM stage 1 was 244.95, reflecting a 4.97% reduction compared with the standard-dose CACS CT (257.75). The mean scores for stages 2 and 3 were 246.86 (4.23% decrease) and 246.14 (4.50% decrease), respectively. Although applying the algorithm induced a slight downward trend in the calcification scores, these deviations were not statistically significant (p = 0.887, 0.919, and 0.685, respectively). Conversely, the median CACS for FNLM stage 1 was 219.15, representing a 14.2% increase over the median standard dose (191.92). This upward shift in the central tendency persisted across stages 2 and 3, with median values of 223.35 (16.4% increase) and 216.85 (13.0% increase), respectively.

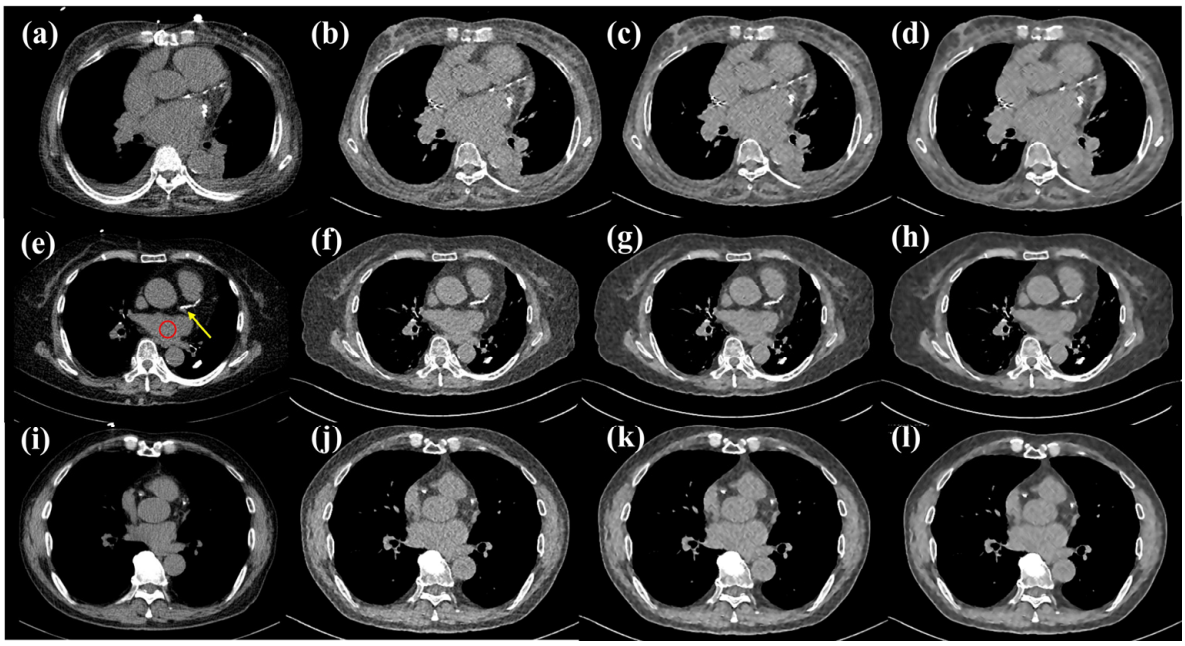


Figure 1. Axial coronary artery calcium score images from three representative patients categorized by heart rate group. (**a**–**d**) Images from the low-heart rate group (HR < 60 bpm), (**e**–**h**) from the mid-heart rate group (60 ≤ HR < 80 bpm), (**i**–**l**) from the high-heart rate group (HR ≥ 80 bpm). Panels (**a**,**e**,**i**) display 3 mm axial images from the standard ECG-gated CACS CT scan. Panels (**b**,**f**,**j**), (**c**,**g**,**k**), and (**d**,**h**,**l**) show 1 mm axial images from non-gated low-dose CT scans post-processed using fast non-local means at levels 1, 2, and 3, respectively. Notably, in the mid-heart rate group (**e**–**h**), the coronary calcifications in the left main and left anterior descending arteries (yellow arrows), remain consistently visible regardless of the fast non-local means strength, suggesting robust preservation of calcified lesions across filtering levels.

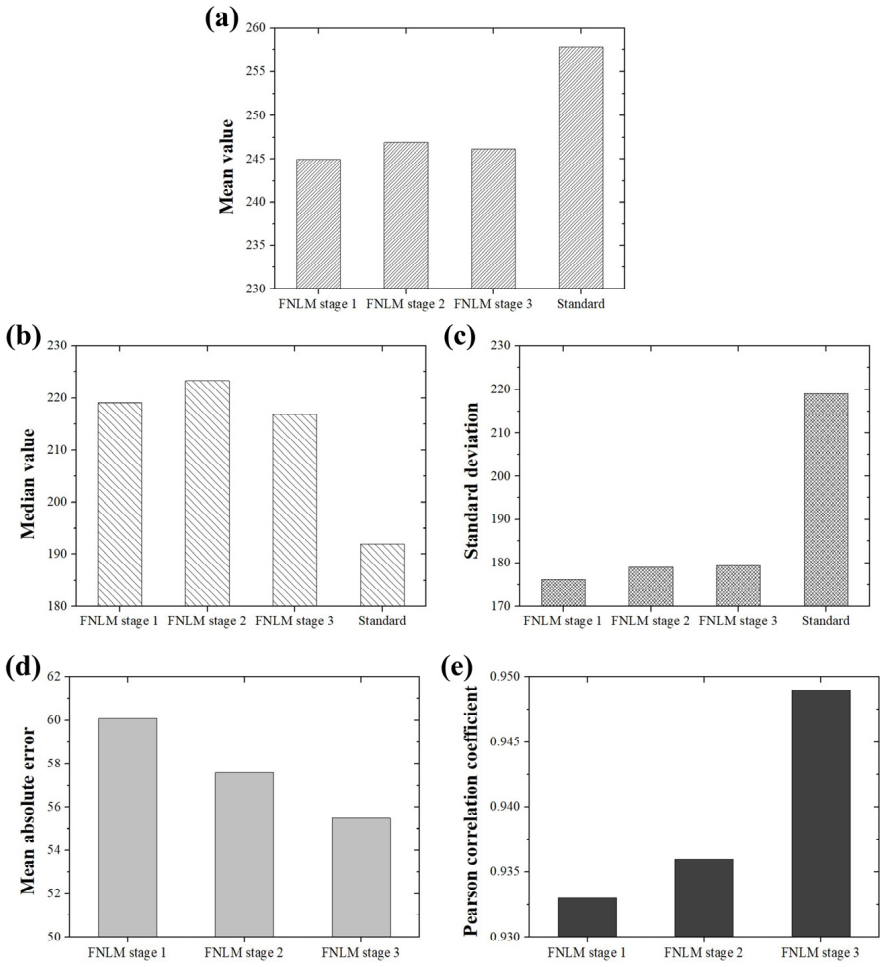


Figure 2. Comparison of calcium scoring metrics between standard-dose and low-dose CT post-processed using fast non-local means at levels 1, 2, and 3. (**a**) The mean, (**b**) median, (**c**) standard deviation of the coronary artery calcium score, (**d**) mean absolute error, and (**e**) Pearson correlation coefficient were calculated to assess quantitative accuracy and consistency between the standard reference and fast non-local means-processed low-dose images.

The standard deviation of the CACS, an indicator of quantitative variability, demonstrated a stable downward trend after post-processing (Figure 2). Compared with the standard-dose CACS CT (219.02), the standard deviation dropped to 176.18 in FNLM stage 1 (19.5% reduction), 179.05 in stage 2 (18.3% reduction), and 179.39 in stage 3 (18.1% reduction). In terms of absolute accuracy, MAE improved progressively with higher algorithm intensity, decreasing from 60.08 in FNLM stage 1 to 57.58 in stage 2, and finally to 55.48 in stage 3.

Pearson correlation analysis confirmed the exceptional consistency between the FNLM-applied low-dose images and standard-dose CACS CT. The correlation coefficients were 0.933, 0.936, and 0.949 for stages 1, 2, and 3, respectively, indicating a highly significant linear relationship ($p < 0.001$). The correlation coefficients progressively improved as the algorithm strength increased; notably, stage 3 exhibited a 1.71% increase over stage 1, demonstrating the highest quantitative agreement with the standard-dose CACS CT images.

3.2. Quantitative Analysis by Vessel

The quantitative impact of the FNLM algorithm was further evaluated on a per-vessel basis across the major coronary arteries. Specifically, the mean CACS and MAE derived from FNLM stages 1–3 were compared with those of the standard-dose images for LM, LAD, CX, and RCA.

For LM (Figure 3), the mean CACS across FNLM stages 1–3 were 39.44, 50.56, and 45.79, respectively, compared to a 54.01 in standard-dose CACS CT. This reflects a consistent and statistically significant downward trend (stage 1, $p = 0.0027$; stage 2, $p = 0.1072$; and stage 3, $p = 0.0215$). The corresponding MAE values were 25.42 (stage 1), 18.36 (stage 2), and 21.53 (stage 3), with significant differences observed at every stage.

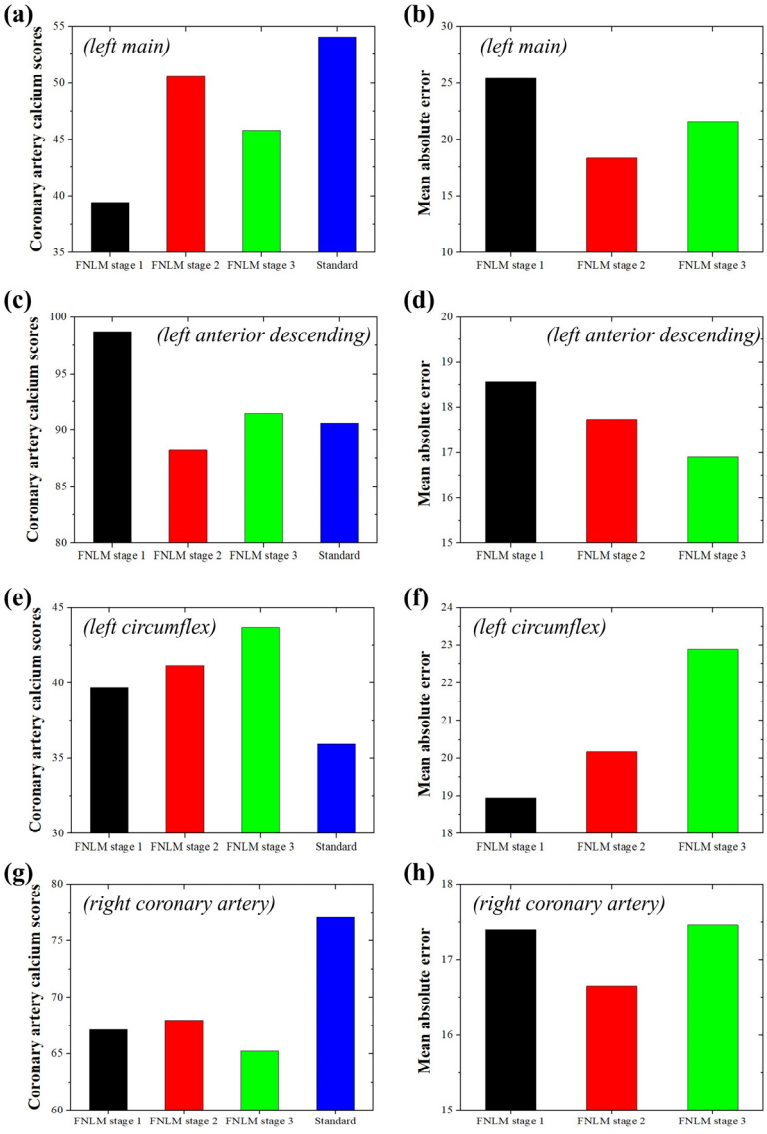


Figure 3. Vessel-specific comparison of coronary artery calcium scores between standard-dose and low-dose CT post-processed using fast non-local means at levels 1, 2, and 3. The bar graphs show the mean CACS (**a**,**c**,**e**,**g**) and mean absolute error (**b**,**d**,**f**,**h**) for each coronary artery: left main, left anterior descending, left circumflex, and right coronary artery. The quantitative differences across filter levels allow the assessment of the accuracy and consistency of fast non-local means applied to low-dose images compared to the standard reference for each vessel.

As illustrated in Figure 3, for LAD, the mean CACS across FNLM stages 1–3 were 98.68, 88.20, and 91.46, respectively, compared with 90.60 in standard-dose CACS CT. These values demonstrated no specific trend across all stages compared with standard-dose CACS CT (stage 1, $p = 0.3754$; stage 2, $p = 0.7247$; and stage 3, $p = 0.8067$). The MAE was 18.57 for stage 1, 17.74 for stage 2, and 16.91 for stage 3, with no statistically significant differences across all stages.

As illustrated in Figure 3, for CX, the scores across FNLM stages 1–3 were 39.68, 41.13, and 43.70, respectively, compared with 35.98 in standard-dose CACS CT. These scores showed an increasing trend across all stages compared with the standard-dose CACS CT (stage 1, $p = 0.0067$; stage 2, $p = 0.0045$; and stage 3, $p = 0.0015$). The MAE was 18.95 for stage 1, 20.17 for stage 2, and 22.89 for stage 3, increasing as the stage increased. All the stages demonstrated statistically significant differences.

As illustrated in Figure 3, for RCA, the mean scores across FNLM stages 1–3 were 67.16, 67.98, and 65.21, respectively, compared with 77.16 in standard-dose CACS images. These scores showed a decreasing trend across all stages compared to standard-dose CACS CT (stage 1, $p = 0.0376$; stage 2, $p = 0.0327$; stage 3, $p = 0.032$). The MAE was 17.40 for stage 1, 16.65 for stage 2, and 17.46 for stage 3.

3.3. Calcium Score Comparison by Heart Rate Group

Based on heart rate, the subjects were divided into three groups (low, <60 bpm; intermediate, 60–80 bpm; high, >80 bpm), and MAE and correlation analyses were performed between the FNLM-processed low-dose chest CT images and standard-dose CACS CT images. In the low heart rate group (Figure 4), MAE decreased sequentially with increasing FNLM intensity: 66.82 for stage 1, 64.75 for stage 2, and 54.91 for stage 3. The Pearson correlation coefficient improved across stages (stage 1, 0.8766; stage 2, 0.8763, and stage 3, 0.9304). However, the absolute CACS disparities between the FNLM and standard-dose images were not statistically significant ($p < 0.05$).

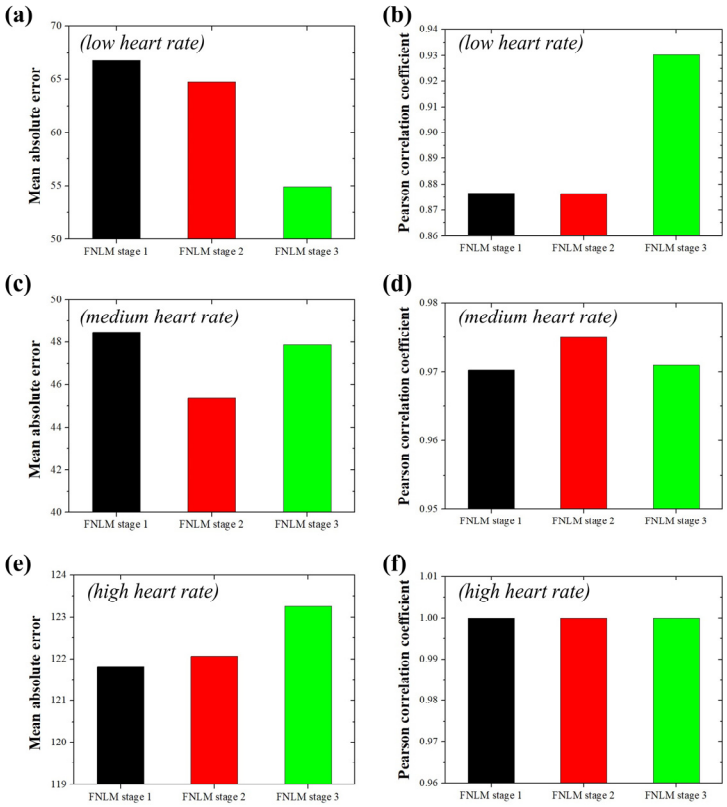


Figure 4. Vessel heart rate-specific comparison of coronary artery calcium scoring performance metrics for low-dose CT images processed with fast non-local means at levels 1, 2, and 3. The bar graphs display the mean absolute (**a**,**c**,**e**) and Pearson correlation coefficient (**b**,**d**,**f**) for the three heart rate groups: low HR (<60 bpm, top row), medium HR (60–79 bpm, middle row), and high HR (≥80 bpm, bottom row). This analysis highlights the impact of fast non-local means strength on scoring accuracy and consistency across varying cardiac motion conditions.

In the intermediate heart rate group, the MAE was 48.46 for FNLM stage 1, 45.35 for stage 2, and 47.88 for stage 3, which was the lowest among the three heart rate groups. The correlation coefficients were exceptionally high (stage 1, 0.9703; stage 2, 0.9750; and stage 3, 0.9710); however, similar to the low heart rate group, statistically significant differences were not detected ($p < 0.05$).

In the high heart rate group, MAE was 121.81 for FNLM stage 1, 122.06 for stage 2, and 123.26 for stage 3, exhibiting the largest error among the three groups. Although the Pearson correlation coefficients was 1.0 for all stages, no statistically significant differences in CACS were found between the FNLM and standard-dose images at any stage ($p > 0.05$).

3.4. Radiation Dose Comparison Analysis

The FNLM-processed low-dose CT images showed significantly lower radiation dose values across all metrics compared with standard-dose CACS CT. As illustrated in Figure 5, mean CTDIvol decreased from 1.969 mGy in the standard images to 0.567 mGy in the FNLM images, representing a reduction of 71.2%. Similarly, the mean DLP fell from 55.77 mGy·cm to 24.26 mGy·cm, achieving a 56.5% decrease. Both reductions were highly significant ($p = 0.001$). Additionally, the Pearson correlation coefficients between the dose reduction rates and absolute error of the CACS pooled across all FNLM stages were −0.07 for CTDIvol and −0.01 for DLP. These results demonstrate a negligible correlation between the radiation dose reduction and CACS error.

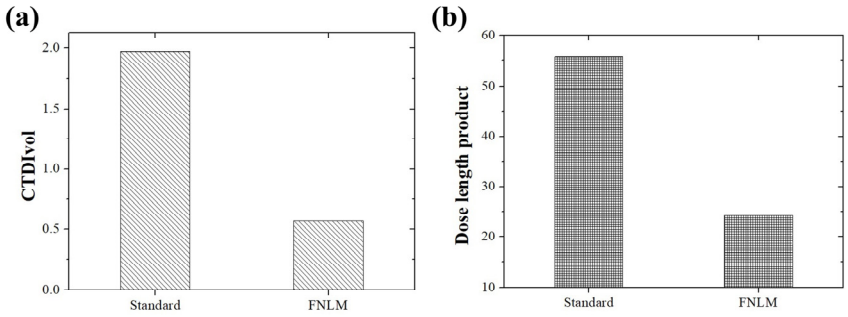


Figure 5. Comparison of radiation dose metrics between standard-dose and low-dose CT with fast non-local means post-processing. The bar graphs illustrate the average CT dose index volume (**a**) and dose-length product (**b**) for coronary artery calcium scoring. Fast non-local means-processed low-dose scans demonstrate substantial reductions in radiation exposure compared with the standard protocol, while maintaining quantitative image quality.

4. Discussion

CACS remains one of the most objective and reproducible methodologies for predicting cardiovascular risk in asymptomatic adults. The 2018 American College of Cardiology and American Heart Association guidelines strongly recommend CACS evaluation for intermediate-risk patients to guide preventive cardiovascular strategies [32]. Traditionally, these measurements require standard CT acquisitions equipped with ECG gating, which mandates a baseline level of radiation exposure. Cumulative radiation exposure is a major concern for patients requiring repeated examinations for screening and follow-up. Furthermore, heart rate variations during image acquisition can affect the accuracy of the CACS measurements [33].

Consequently, the evaluation of CACS using low-dose chest CT instead of dedicated cardiac CT has recently gained significant attention [34,35]. To make this viable, various image post-processing algorithms have been introduced. The FNLM algorithm is an advanced nonlinear filter capable of effectively reducing image noise based on repetitive spatial patterns without degrading intricate anatomical borders [36]. Unlike iterative

reconstruction and deep learning-based denoising methods, which are often integrated into vendor-specific reconstruction pipelines, FNLM can be applied as a flexible post-processing technique without requiring dedicated training data or system-specific implementation. In addition, the FNLM algorithm was applied as an offline post-processing step in this study. Although it does not require dedicated training or GPU-based infrastructure, its computational complexity may increase depending on the selected parameters, which could limit real-time clinical application. Further optimization, including parallelization and hardware acceleration, is required to enable integration into routine clinical workflows. Accordingly, we hypothesized that applying the FNLM algorithm to low-dose images with increased noise would suppress extraneous noise while preserving the morphological integrity of the calcifications, thereby maintaining CACS accuracy. Although non-ECG-gated low-dose lung CT is inherently limited by coronary artery motion artifacts resulting from individual heart rate fluctuations, a high-pitch acquisition protocol was used to overcome this technical drawback.

Our findings confirmed that the FNLM algorithm successfully sustained the CACS accuracy in noisy, low-dose CT environments. While applying the algorithm that induced a slight overall reduction in the mean CACS relative to the standard dose, the absence of statistical significance suggests that the underlying quantitative consistency is not fundamentally impaired by the increased noise of the low-dose protocol [37]. Willemink et al. [37] noted that iterative reconstruction (IR) algorithms applied to low-dose CT significantly reduced both the mean CACS and its standard deviation. These results are consistent with our findings, as the implementation of the FNLM reduced both the standard deviation and MAE. Notably, the MAE declined sequentially with higher FNLM intensity, indicating the progressive minimization of the quantitative error. The continuous improvement in the Pearson correlation coefficients across the escalating algorithm stages underscores the critical necessity of protocol optimization when determining the appropriate FNLM strength for clinical deployment.

In this study, changes in CACS across the FNLM stages were analyzed for each vessel (LM, LAD, CX, and RCA). LM and RCA exhibited a CACS reduction compared with standard-dose images, mirroring the overall mean trend. In contrast, the CX vessel displayed a distinct and statistically significant increase in CACS following FNLM. Because CX is characterized by narrower diameters and greater anatomical tortuosity than other major coronary arteries, subjective operator bias likely plays a more prominent role during the scoring process. Given the disparity in clinical experience between our two independent evaluators, subjective interpretation may have disproportionately skewed the assessment of the more complex vascular anatomy. Conversely, LAD showed no significant statistical deviation. Ultimately, these vessel-specific variations confirm that the quantitative impact of FNLM on low-dose imaging is heavily modulated by the local vascular geometry and caliber.

Subgroup analysis based on the heart rate revealed that the high heart rate group exhibited the highest MAE. This can be attributed to the increased motion artifacts at higher heart rates, which obscure lesion boundaries and consequently increase quantitative measurement errors. However, no statistically significant differences were observed across heart rate groups. This demonstrates that utilizing a high-pitch protocol can maintain CACS consistency even under high heart rate conditions without the need for ECG gating. This workflow offers a highly practical alternative for older adult patients or individuals suffering from arrhythmias for whom traditional heart rate regulation is challenging.

Importantly, the substantial radiation dose reduction achieved in this study, with a 71.2% decrease in CTDIvol and a 56.5% decrease in DLP, highlights the clinical feasibility of this approach, particularly for patients requiring repeated imaging or opportunistic

cardiovascular risk assessment. This aligns with the recent conclusions by Groen et al. [38], who posited that reliable CACS evaluations could be extracted from non-gated chest CTs without inflicting supplemental radiation exposure. In this study, the correlation between the dose reduction rate and CACS MAE was negligible, suggesting that dose reduction does not directly compromise quantitative accuracy. These findings highlight the clinical utility of the FNLM algorithm and demonstrate its potential to maintain quantitative accuracy while minimizing cumulative radiation exposure, particularly in high-risk groups or patients requiring repeated scans.

The FNLM algorithm suppresses background noise while accentuating lesion boundaries and preserving structural topology [25]. Although our results demonstrated an aggregate reduction in the quantitative error, they also highlighted the sensitivity of the algorithm. Adjusting the strength of the algorithm directly influences the lesion detection thresholds, indicating that clinical implementation must carefully balance aggressive noise reduction with the retention of fine spatial resolution. Because the efficacy of the algorithm fluctuates based on the vessel diameter and curvature, future optimization efforts must prioritize the development of patient-tailored, anatomically adaptive post-processing profiles. In particular, excessive smoothing may obscure small or low-density calcifications near the detection threshold (e.g., 130 HU), which could potentially affect lesion-level detectability despite the preserved overall quantitative agreement.

This study has several limitations. First, the limited sample size of 30 patients drawn from a single institution restricts generalizability. This limitation is particularly pronounced in the high-heart-rate subgroup, which included only two patients; therefore, the findings from this subgroup lack statistical robustness and should be interpreted with caution; robust validation via larger, multicenter cohorts is essential. Second, the time interval between image acquisitions (up to 6 months) may reflect actual clinical changes. Third, although the proposed framework demonstrated strong quantitative agreement with standard-dose CACS CT, direct comparisons with ECG-gated low-dose CT protocols were not performed, which limits the ability to fully assess the impact of cardiac motion on calcium scoring accuracy. Fourth, while this study demonstrated strong continuous quantitative agreement using metrics such as ICC, Pearson correlation, and MAE, it did not extensively evaluate categorical diagnostic performance, such as cardiovascular risk-category reclassification. Future studies incorporating risk category agreement are warranted to comprehensively validate the clinical diagnostic utility of the FNLM algorithm. Fifth, while the interobserver reliability between the two readers was highly consistent, the assessment was limited to a panel of only two evaluators. Future validations involving a larger, multi-center panel of readers would be beneficial to further eliminate potential subjective bias, especially in anatomically complex vessels. Finally, this study did not include direct comparisons with iterative reconstruction or deep learning-based denoising methods, which limits the ability to fully assess the relative performance of FNLM. Future studies should perform head-to-head comparisons to determine the optimal denoising strategy for low-dose CACS evaluation.

5. Conclusions

This study demonstrates that applying the FNLM algorithm in varying stages to high-pitch, non-ECG-gated, low-dose chest CT demonstrates strong quantitative agreement with standard-dose CACS while facilitating profound radiation dose reduction. These findings suggest that FNLM-processed low-dose chest CT demonstrates strong quantitative agreement with standard-dose CACS CT and may serve as a feasible alternative approach, although further validation is required. Furthermore, the results indicate that FNLM-based

processing may offer a practical approach for CACS evaluation without ECG gating, with the potential to reduce radiation exposure in patients undergoing repeated examinations.

Author Contributions: Conceptualization, J.S. and K.K.; methodology, J.-Y.K. and K.K.; software, K.K.; validation, J.-Y.K.; formal analysis, J.S. and K.K.; investigation, J.S. and J.-Y.K.; writing—original draft preparation, J.S.; writing—review and editing, J.-Y.K. and K.K.; project administration, K.K. All authors have read and agreed to the published version of the manuscript.

Funding: This study was supported by the Wonkwang University in 2026.

Institutional Review Board Statement: The study protocol was approved by the Institutional Review Board of the Yonsei University Health System (Approval No. 4-2024-0123, 28 March 2024).

Informed Consent Statement: Patient consent was waived due to the retrospective nature of the study, and all data used were anonymized.

Data Availability Statement: The raw data supporting the conclusions of this study will be made available by the authors upon request.

Conflicts of Interest: The authors declare no conflicts of interest.

References

1. Greenland, P.; Blaha, M.J.; Budoff, M.J.; Erbel, R.; Watson, K.E. Coronary calcium score and cardiovascular risk. *J. Am. Coll. Cardiol.* **2018**, *72*, 434–447. [CrossRef]
2. Goff, D.C., Jr.; Lloyd-Jones, D.M.; Bennett, G.; Coady, S.; D'Agostino, R.B.; Gibbons, R.; Greenland, P.; Lackland, D.T.; Levy, D.; O'Donnell, C.J.; et al. 2013 ACC/AHA guideline on the assessment of cardiovascular risk: A report of the American College of Cardiology/American Heart Association Task Force on Practice Guidelines. *J. Am. Coll. Cardiol.* **2014**, *63*, 2935–2959. [CrossRef]
3. Piepoli, M.F.; Hoes, A.W.; Agewall, S.; Albus, C.; Brotons, C.; Catapano, A.L.; Cooney, M.-T.; Corrà, U.; Cosyns, B.; Deaton, C.; et al. 2016 European Guidelines on cardiovascular disease prevention in clinical practice: The Sixth Joint Task Force of the European Society of Cardiology and Other Societies on cardiovascular Disease Prevention in Clinical Practice (constituted by representatives of 10 societies and by invited experts): Developed with the special contribution of the European Association for Cardiovascular Prevention & Rehabilitation (EACPR). *Eur. J. Prev. Cardiol.* **2016**, *37*, 2315–2381.
4. Hecht, H.S.; Cronin, P.; Blaha, M.J.; Budoff, M.J.; Kazerooni, E.A.; Narula, J.; Yankelevitz, D.; Abbara, S. 2016 SCCT/STR guidelines for coronary artery calcium scoring of noncontrast noncardiac chest CT scans: A report of the Society of Cardiovascular Computed Tomography and Society of Thoracic Radiology. *J. Cardiovasc. Comput. Tomogr.* **2017**, *11*, 74–84. [CrossRef]
5. Hughes-Austin, J.M.; Dominguez, A.; Allison, M.A.; Wassel, C.L.; Rifkin, D.E.; Morgan, C.G.; Daniels, M.R.; Ikram, U.; Knox, J.B.; Wright, C.M.; et al. Relationship of coronary calcium on standard chest CT scans with mortality. *JACC Cardiovasc. Imaging* **2016**, *9*, 152–159. [CrossRef]
6. Jacobs, P.C.; Prokop, M.; van der Graaf, Y.; Gondrie, M.J.; Janssen, K.J.; de Koning, H.J.; Isgum, I.; van Klaveren, R.J.; Oudkerk, M.; van Ginneken, B.; et al. Comparing coronary artery calcium and thoracic aorta calcium for prediction of all-cause mortality and cardiovascular events on low-dose non-gated computed tomography in a high-risk population of heavy smokers. *Atherosclerosis* **2010**, *209*, 455–462. [CrossRef]
7. Mets, O.M.; Vliegenthart, R.; Gondrie, M.J.; Viergever, M.A.; Oudkerk, M.; de Koning, H.J.; Mali, W.P.; Prokop, M.; van Klaveren, R.J.; van der Graaf, Y.; et al. Lung cancer screening CT-based prediction of cardiovascular events. *JACC Cardiovasc. Imaging* **2013**, *6*, 899–907. [CrossRef]
8. Chiles, C.; Duan, F.; Gladish, G.W.; Ravenel, J.G.; Baginski, S.G.; Snyder, B.S.; DeMello, S.; Desjardins, S.S.; Munden, R.F.; NLST Study Team. Association of coronary artery calcification and mortality in the national lung screening trial: A comparison of three scoring methods. *Radiology* **2015**, *276*, 82–90. [CrossRef] [PubMed]
9. Arnett, D.K.; Blumenthal, R.S.; Albert, M.A.; Buroker, A.B.; Goldberger, Z.D.; Hahn, E.J.; Himmelfarb, C.D.; Khera, A.; Lloyd-Jones, D.; McEvoy, J.W.; et al. 2019 ACC/AHA Guideline on the Primary Prevention of cardiovascular Disease: A report of the American College of Cardiology/American Heart Association Task Force on Clinical Practice Guidelines. *Circulation* **2019**, *140*, e596–e646. [CrossRef] [PubMed]
10. Kim, K.P.; Einstein, A.J.; Berrington de González, A.B. Coronary artery calcification screening: Estimated radiation dose and cancer risk. *Arch. Intern. Med.* **2009**, *169*, 1188–1194. [CrossRef] [PubMed]
11. Valente, D.; Gentileschi, M.P.; Valenti, A.; Burgio, M.; Soddu, S.; Bruzzaniti, V.; Guerrisi, A.; Verdina, A. Cumulative dose from recurrent CT scans: Exploring the DNA damage response in human non-transformed cells. *Int. J. Mol. Sci.* **2024**, *25*, 7064. [CrossRef]

12. Haubenreisser, H.; Meyer, M.; Sudarski, S.; Allmendinger, T.; Schoenberg, S.O.; Henzler, T. Unenhanced third-generation dual-source chest CT using a tin filter for spectral shaping at 100 kVp. *Eur. J. Radiol.* **2015**, *84*, 1608–1613. [CrossRef] [PubMed]
13. Gordic, S.; Morsbach, F.; Schmidt, B.; Allmendinger, T.; Flohr, T.; Husarik, D.; Baumueller, S.; Raupach, R.; Stolzmann, P.; Leschka, S.; et al. Ultralow-dose chest computed tomography for pulmonary nodule detection: First performance evaluation of single energy scanning with spectral shaping. *Investig. Radiol.* **2014**, *49*, 465–473. [CrossRef]
14. Sagara, Y.; Hara, A.K.; Pavlicek, W.; Silva, A.C.; Paden, R.G.; Wu, Q. Abdominal CT: Comparison of low-dose CT with adaptive statistical iterative reconstruction and routine-dose CT with filtered back projection in 53 patients. *Am. J. Roentgenol.* **2010**, *195*, 713–719. [CrossRef] [PubMed]
15. Kim, W.; Jeon, S.-Y.; Byun, G.; Yoo, H.; Choi, J.-H. A systematic review of deep learning-based denoising for low-dose computed tomography from a perceptual quality perspective. *Biomed. Eng. Lett.* **2024**, *14*, 1153–1173. [CrossRef]
16. Blobel, J.; Mews, J.; Schuijf, J.D.; Overlaet, W. Determining the radiation dose reduction potential for coronary calcium scanning with computed tomography: An anthropomorphic phantom study comparing filtered backprojection and the adaptive iterative dose reduction algorithm for image reconstruction. *Investig. Radiol.* **2013**, *48*, 857–862. [CrossRef]
17. Tesche, C.; De Cecco, C.N.; Schoepf, U.J.; Duguay, T.M.; Albrecht, M.H.; Caruso, D.; Varga-Szemes, A.; Lesslie, V.W.; Ebersberger, U.; Canstein, C.; et al. Iterative beam-hardening correction with advanced modeled iterative reconstruction in low voltage CT coronary calcium scoring with tin filtration: Impact on coronary artery calcium quantification and image quality. *J. Cardiovasc. Comput. Tomogr.* **2017**, *11*, 354–359. [CrossRef]
18. Allio, I.R.; Caobelli, F.; Popescu, C.E.; Haaf, P.; Alberts, I.; Frey, S.M.; Zellweger, M.J. Low-dose coronary artery calcium scoring compared to the standard protocol. *J. Nucl. Cardiol.* **2023**, *30*, 1191–1198. [CrossRef] [PubMed]
19. Dobrolinska, M.M.; van Praagh, G.D.; Oostveen, L.J.; Poelhekken, K.; Greuter, M.J.W.; Fleischmann, D.; Willemink, M.J.; de Lange, F.; Slart, R.H.J.A.; Leiner, T.; et al. Systematic assessment of coronary calcium detectability and quantification on four generations of CT reconstruction techniques: A patient and phantom study. *Int. J. Cardiovasc. Imaging* **2023**, *39*, 221–231. [CrossRef]
20. Zhang, H.; Zeng, D.; Zhang, H.; Wang, J.; Liang, Z.; Ma, J. Applications of nonlocal means algorithm in low-dose X-ray CT image processing and reconstruction: A review. *Med. Phys.* **2017**, *44*, 1168–1185. [CrossRef]
21. Zhao, T.; Hoffman, J.; McNitt-Gray, M.; Ruan, D. Ultra-low-dose CT image denoising using modified BM3D scheme tailored to data statistics. *Med. Phys.* **2019**, *46*, 190–198. [CrossRef] [PubMed]
22. Shim, J.; Kang, S.-H.; Lee, Y. Utility of block-matching and 3D filter for reproducibility of lung density and denoising in low-dose chest CT: A pilot study. *Phys. Med.* **2024**, *124*, 103432. [CrossRef]
23. Buades, A.; Coll, B.; Morel, J.M. A review of image denoising algorithms, with a new one. *Multiscale Model. Simul.* **2005**, *4*, 490–530. [CrossRef]
24. Kim, B.-G.; Kang, S.-H.; Park, C.R.; Jeong, H.-W.; Lee, Y. Noise level and similarity analysis for computed tomographic thoracic image with fast non-local means denoising algorithm. *Appl. Sci.* **2020**, *10*, 7455. [CrossRef]
25. Shim, J.; Kim, K.; Lee, Y. Improving the accuracy of coronary artery calcium scoring in computed tomography images using a fast nonlocal means noise-reduction algorithm. *Biomed. Signal Process. Control* **2026**, *120*, 110155. [CrossRef]
26. Bischoff, B.; Meinel, F.G.; Del Prete, A.; Reiser, M.F.; Becker, H.-C. High-pitch coronary CT angiography in dual-source CT during free breathing vs. breath holding in patients with low heart rates. *Eur. J. Radiol.* **2013**, *82*, 2217–2221. [CrossRef] [PubMed]
27. Baumueller, S.; Alkadhi, H.; Stolzmann, P.; Frauenfelder, T.; Goetti, R.; Schertler, T.; Plass, A.; Falk, V.; Feuchtner, G.; Scheffel, H.; et al. Computed tomography of the lung in the high-pitch mode: Is breath holding still required? *Investig. Radiol.* **2011**, *46*, 240–245. [CrossRef]
28. Schulz, B.; Jacobi, V.; Beeres, M.; Bodelle, B.; Gruber, T.; Lee, C.; Bauer, R.; Kerl, M.; Vogl, T.; Zangos, S. Quantitative analysis of motion artifacts in high-pitch dual-source computed tomography of the thorax. *J. Thorac. Imaging* **2012**, *27*, 382–386. [CrossRef]
29. Lell, M.M.; May, M.; Deak, P.; Alibek, S.; Kuefner, M.; Kuettner, A.; Köhler, H.; Achenbach, S.; Uder, M.; Radkow, T. High-pitch spiral computed tomography: Effect on image quality and radiation dose in pediatric chest computed tomography. *Investig. Radiol.* **2011**, *46*, 116–123. [CrossRef]
30. Dauwe, A.; Goossens, B.; Luong, H.Q.; Philips, W. A fast non-local image denoising algorithm. *Image Process. Algor. Syst.* **2008**, *6812*, 681210. [CrossRef]
31. Kim, H.; Park, J.; Shim, J.; Lee, Y. Application and optimization of a fast non-local means noise reduction algorithm in pediatric abdominal virtual monoenergetic images. *Electronics* **2024**, *13*, 4684. [CrossRef]
32. Grundy, S.M.; Stone, N.J.; Bailey, A.L.; Beam, C.; Birtcher, K.K.; Blumenthal, R.S.; Braun, L.T.; de Ferranti, S.; Faiella-Tommasino, J.; Forman, D.E.; et al. 2018 AHA/ACC/AACVPR/AAPA/ABC/ACPM/ADA/AGS/APhA/ASPC/NLA/PCNA guideline on the management of blood cholesterol: Executive summary: A report of the American College of Cardiology/American Heart Association Task Force on Clinical Practice guidelines. *Circulation* **2019**, *139*, e1046–e1081. [CrossRef]
33. Kędzierski, B.; Macek, P.; Dziadkowiec-Macek, B.; Truszkiewicz, K.; Poręba, R.; Gać, P. Radiation doses in cardiovascular computed tomography. *Life* **2023**, *13*, 990. [CrossRef] [PubMed]

34. Takx, R.A.P.; de Jong, P.A.; Leiner, T.; Oudkerk, M.; de Koning, H.J.; Mol, C.P.; Viergever, M.A.; Išgum, I. Automated coronary artery calcification scoring in non-gated chest CT: Agreement and reliability. *PLoS ONE* **2014**, *9*, e91239. [CrossRef] [PubMed]
35. Choi, J.H.; Cha, M.J.; Cho, I.; Kim, W.D.; Ha, Y.; Choi, H.; Lee, S.H.; You, S.C.; Chang, J.S. Validation of deep learning-based fully automated coronary artery calcium scoring using non-ECG-gated chest CT in patients with cancer. *Front. Oncol.* **2022**, *12*, 989250. [CrossRef]
36. Kim, H.; Lim, S.; Park, M.; Kim, K.; Kang, S.-H.; Lee, Y. Optimization of fast non-local means noise reduction algorithm parameter in computed tomographic phantom images using 3D printing technology. *Diagnostics* **2024**, *14*, 1589. [CrossRef] [PubMed]
37. Willemink, M.J.; Takx, R.A.P.; de Jong, P.A.; Budde, R.P.J.; Bleys, R.L.A.W.; Das, M.; Wildberger, J.E.; Prokop, M.; Buls, N.; de Mey, J.; et al. The impact of CT radiation dose reduction and iterative reconstruction algorithms from four different vendors on coronary calcium scoring. *Eur. Radiol.* **2014**, *24*, 2201–2212. [CrossRef]
38. Groen, R.A.; Jukema, J.W.; van Dijkman, P.R.M.; Bax, J.J.; Lamb, H.J.; Antoni, M.L.; de Graaf, M.A. The clear value of coronary artery calcification evaluation on non-gated chest computed tomography for cardiac risk stratification. *Cardiol. Ther.* **2024**, *13*, 69–87. [CrossRef]

Disclaimer/Publisher's Note: The statements, opinions and data contained in all publications are solely those of the individual author(s) and contributor(s) and not of MDPI and/or the editor(s). MDPI and/or the editor(s) disclaim responsibility for any injury to people or property resulting from any ideas, methods, instructions or products referred to in the content.